KFUPM
Journal of Undergraduate Research International

Diamond Open Access 24

Article Chemical Engineering

Electrochemical Deposition of Mono- and Bi-metallic Ni-Cu Electrodes for 5-Hydroxymethylfurfural Oxidation to 2,5-Furandicarboxylic Acid

Hussa Naji Alwohaibi and Wasif Farooq*

Cite https://doi.org/10.64589/juri/231583

Submitted: April 25, 2026 **Revised:** May 09, 2026 **Accepted:** May 15, 2026

ABSTRACT

The electrochemical oxidation of biomass-derived molecules has gained attention as a sustainable route for producing value-added chemicals. In this study, Ni- and Cu-based catalysts for the electrochemical oxidation of 5-hydroxymethylfurfural (HMF) to 2,5-furandicarboxylic acid (FDCA) were synthesized using different electrodeposition techniques, including single-metal, mixed-metal, and layer-by-layer deposition, to evaluate their influence on electrocatalytic activity. Key parameters of the electrodeposition process were systematically studied by varying the precursor volume, applied potential, and deposition mode. Structural characterization confirmed differences in morphology and metal distribution across the prepared samples. The Ni–Cu-based electrodes, particularly those prepared via mixed and LBL deposition, exhibited enhanced activity compared with the single-metal electrodes. The optimized Ni–Cu LBL electrode exhibited higher current densities for HMF oxidation (~0.20 A cm^{-2} at ~1.80 V vs. the reversible hydrogen electrode) and a lower onset potential relative to the O_2 evolution reaction, indicating improved catalytic activity. Moreover, this electrode achieved approximately 95% HMF conversion after 120 min, along with an FDCA yield of approximately 50%. This low FDCA yield indicates the possible formation of other intermediates or side products. Overall, this study demonstrates that catalyst composition, deposition strategy, and operational parameters play critical roles in the design of effective transition-metal-based electrocatalysts for HMF oxidation.

Keywords: biomass-derived, HMF, FDCA, electrochemical oxidation, metal oxides

1. INTRODUCTION

The global dependence on fossil fuels has steadily increased because of their central role in the chemical industry[1], where they serve as primary feedstocks for fuels[2,3], polymers[4,5], solvents, and other value-added chemicals[4,6]. Petroleum-based fuels are not only a major source of energy[7] but also fundamental raw materials used in a wide range of chemical products[8,9]. However, the reliance on such fuels is associated with high carbon emissions[10,11], which contribute to climate change.[12,13], air pollution[14], and long-term environmental degradation[15–17], including ecosystem disruption and waste accumulation[18]. These concerns are not limited to fuel consumption alone, the production of chemicals and materials has emerged as an equally critical issue[9,19]. However, as a nonrenewable resource utilized across multiple industrial sectors, the extensive use of petroleum has placed growing pressure on researchers and industries to develop cleaner and more sustainable alternatives[20,21]. In response to these challenges, the transition toward sustainable chemical production has become a necessity rather than a choice or luxury.

Biomass-derived compounds are widely considered promising alternatives to fossil-fuel-based carbon for chemical production[22–24]. Biomass offers significant advantages as a renewable and sustainable carbon source[25]. During growth, biomass feedstocks absorb CO_2 from the atmosphere, generating renewable carbon. This renewable carbon can then be utilized as feedstock for chemical synthesis, supporting the development of more sustainable production routes[26]. 5-Hydroxymethylfurfural (HMF)[27,28] is a biomass-derived compound ranked among the top 10 candidates for replacing petroleum-based compounds[29]. HMF oxidation produces 2,5-furandicarboxylic acid (FDCA), another major biomass-derived compound. These compounds are often referred to as "sleeping giants" because of their unique position between petroleum-based and carbohydrate chemistry[29–31]. FDCA has gained particular interest because it can be used in the production of polyethylene furanoate, a bio-based polyester, and as a sustainable alternative to polyethylene terephthalate (PET)[32]. Plastics are widely utilized in everyday life, leading to a continuous increase in production demand[33]. PET, for example, is one of the most extensively used polymers in various plastic applications. However, petroleum-based plastics are primarily synthesized from fossil resources and are difficult to dispose[34,35]. Despite the potential of FDCA as a bio-based building block for sustainable plastics, its production remains a major challenge.

Various catalytic systems, such as homogeneous catalysts[36], heterogeneous catalysts[37], thermocatalytic oxidation systems,

Published under an exclusive license by KFUPM

and electrochemical oxidation systems, have been developed to enable the effective oxidation of HMF to FDCA. Thermocatalytic approaches, such as the Ni–Cu bimetallic oxide system reported by Xing et al., can achieve FDCA yields of 93.46% by employing oxygen vacancies and metal interfaces to enhance oxygen transfer and adsorption.[38]. Electrochemical oxidation systems[39–45] use electricity to drive the HMF oxidation reaction (HMFOR) under mild conditions; the oxidation reaction at the anode may also be coupled with H_2 evolution at the cathode, enabling the simultaneous production of FDCA and H_2 as a clean fuel[46]. This technology has opened opportunities for researchers to implement electrochemical reactions as an effective approach for HMF conversion. Among the various electrocatalysts investigated to date, transition-metal-based materials, particularly Ni- and Cu-based systems, have attracted significant attention owing to their low cost and promising activity. Yang et al. reported that $Ni(OH)_2$ nanosheets supported on Ni foam exhibit high HMF conversion ability and selectivity[41].

Similarly, Zhang et al. developed $Ni_{0.9}Cu_{0.1}(OH)_2$ nanosheets that could achieve an FDCA yield of 91.2%; here, both the NiOOH active species and Cu incorporation improved the catalytic behavior of the material[39]. Bimetallic Ni–Cu systems also show significant promise. Li et al. constructed a Ni–Cu heterostructured catalyst capable of operating at industrial current densities with a Faradaic efficiency exceeding 98%[40]. Hou et al. reported a Ni–Cu catalyst exhibiting high activity and stability owing to the interaction between Cu_2O and $Ni(OH)_2$ phases[42]. In addition, Liu et al. demonstrated a Ni–Cu alloy catalyst capable of nearly complete conversion and an FDCA yield of up to 99.8%; Cu improved the conductivity of the catalyst and stabilized the Ni active sites[43]. The reaction mechanism discussed by Woo et al. revealed that NiOOH and $Cu(OH)_2$ play complementary roles, with Ni facilitating alcohol oxidation and Cu promoting aldehyde oxidation, thereby enabling efficient sequential conversion to FDCA[44].

Despite the progress in this field, the available catalytic systems still present several limitations. Thermocatalytic approaches generally require high temperatures and long reaction times, leading to increased energy consumption and reduced sustainability. In electrochemical systems, catalytic performance strongly depends on the formation and stability of the active sites of species such as NiOOH, which may undergo surface reconstruction during operation, affecting long-term stability. The activity of Ni- and Cu-based catalysts is highly influenced by their surface composition and oxidation state, rendering their catalytic behavior sensitive to the operating conditions. Although improved performance has been reported for Ni–Cu bimetallic systems, their activity largely depends on the interaction between Ni and Cu species, as well as their distribution on the catalyst surface, which requires careful control during synthesis. Therefore, achieving a simple and controllable system with stable performance remains challenging.

A simple and controllable strategy for tuning the composition and interactions of Ni–Cu-based catalysts is essential for their successful development. In this study, Ni-, Cu-, and Ni–Cu-based catalysts for HMFOR were prepared via direct electrodeposition on Ni foam as a conductive substrate. Figure 1 illustrate the experimental setup employed in this study. The following part present the methodology including materials used, the preparation of the electrodes through different electrodeposition configurations, the electrochemical measurements, morphological characterization, and product analysis methods. The subsequent section discusses the corresponding experimental results, including catalyst characterization, electrochemical performance, HPLC product analysis and long-term stability. Finally, the paper conclude with the main findings of this study.

2. EXPERIMENTAL PROCEDURES

2.1. Materials and Chemicals. $Ni(NO_3)_2 \cdot 6H_2O$ (≥97%, Sigma–Aldrich, Germany) and $Cu(NO_3)_2 \cdot 3H_2O$ (99%–104%, Sigma–Aldrich, Spain) were used as metal precursors for catalyst fabrication. HMF (99%, Sigma–Aldrich, USA) was used as the model biomass-derived substrate for the electrooxidation experiments. KOH pellets (≥85%, AnalaR, BDH Chemicals Ltd., UK) were used to prepare the alkaline electrolyte. Ni foam (75 pores per inch (ppi), 2 mm thickness) was employed as the conductive substrate and working electrode support. All chemicals were of analytical grade and used as received without further purification. Deionized (DI) water was used to prepare all the solutions.

2.2. Pre-treatment of the Ni Foam. The Ni foam was cut into pieces measuring 2cm × 1cm. The samples were rinsed with double-distilled water to remove surface dust, immersed in a 1.0 M HCl solution, and ultrasonicated for 20 min in an ultrasonic bath to remove surface oxides and impurities. After acid treatment, the samples were thoroughly rinsed with double-distilled water, immersed in ethanol, and ultrasonicated for 20 min to eliminate residual organic contaminants. Finally, the samples were rinsed with double-distilled water and dried in an oven at 45–65 °C for 1 h prior to use.

2.3. Preparation of the Electrodes. Electrodeposition was performed using a three-electrode configuration with Ni foam as the working electrode, Pt as the counter electrode, and Ag/AgCl as the reference electrode. An initial optimization study was performed to evaluate the effects of the deposition time, applied potential, and precursor concentration on the electrocatalytic performance of the resulting catalysts. Structural and morphological characterizations were also performed.

2.3.1. Preparation of the precursor solution. Stock solutions (0.5 M) of Cu and Ni were prepared for metal deposition. Different volumes of the stock solution (2, 4, and 6 mL) were mixed with DI water to reach a total volume of 19 mL, yielding precursor solutions with final concentrations of 0.053, 0.105, and 0.158 M. The pH of the solutions was measured before and after the deposition of each layer to monitor pH changes during the process.

2.3.2. Deposition of Cu and Ni. The Ni foam substrate was weighed before and after the deposition of each metal layer to monitor changes in mass. The applied potential was optimized by testing different values (−0.5, −1.0, −1.5, and −2.0 V vs. Ag/AgCl) to determine the most suitable condition for the electrodeposition of each metal.

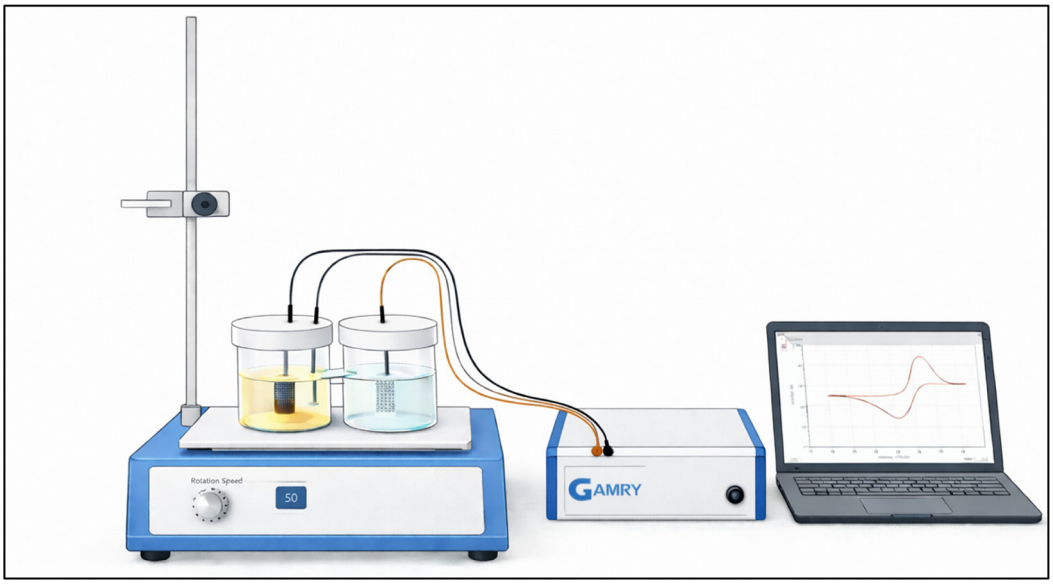


Figure 1. Schematic illustration of the electrochemical cell setup used for electrode preparation and electrochemical oxidation

2.3.3. Preparation of electrodes with different configurations. Electrodes with different configurations were prepared to compare the effects of different electrodeposition methods. Single-metal, mixed-metal, and LBL deposition beginning with either Ni or Cu was performed using optimized concentrations of Cu and Ni. All electrodeposition procedures were performed using a chronoamperometric method controlled by a Gamry potentiostat. A constant potential of −2.0 V was applied, and the resulting current response was monitored over time.

Metal deposition was performed for 120 s per layer to ensure consistent film formation and controlled growth on the Ni foam substrate. For LBL deposition, the same procedure was repeated for the second metallic layer. For some electrodes, the deposition time was extended to increase the thickness and surface coverage of a specific metal layer, thereby allowing the investigation of the effect of layer dominance on the catalyst structure and composition.

2.4. Preparation of the HMF Stock Solution. A 100 mM HMF stock solution was prepared by weighing the required amount of HMF and completely dissolving it in DI water. During the electrochemical measurements, 3 mL of the HMF stock solution was added to the H-cell by replacing an equal volume of the KOH electrolyte to maintain a constant total volume. After mixing inside the cell, the HMF solution was diluted to a final concentration of 10 mM.

2.5. Evaluation of the Conversion of HMF to FDCA. An H-cell was used for the electrocatalytic conversion of HMF to FDCA. Both compartments of the cell contained equal amounts (30 mL) of 1.0 M KOH. The two chambers were separated by a Nafion-117 membrane. Cyclic voltammetry (CV) was performed for 50 cycles to activate the electrode surface, followed by an additional 5–10 cycles to ensure a stable response before further measurements.

After stabilization, LSV was conducted by sweeping the potential to −1.5 V vs. Ag/AgCl and recording the current response. Under these conditions, the measured current mainly corresponds to the OER in alkaline solution, thereby providing a reference for comparison after the introduction of HMF. EIS was conducted to evaluate the charge-transfer behavior at the electrode surface under the same conditions.

The open-circuit potential (OCP) was subsequently recorded for 600 s: measurements over the first 300 s were conducted without HMF, while those over the next 300 s were conducted after replacing 3 mL of KOH with the 10 mM HMF solution while maintaining a constant total volume of 30 mL. This process allowed the direct observation of changes in surface interactions after the introduction of HMF.

LSV was performed once more in the presence of 3 mM HMF to evaluate the electrocatalytic behavior of the electrodes toward HMFOR, followed by EIS measurements to compare the charge transfer behavior before and after HMF addition.

2.6. Structural and Morphological Characterization. The surface structures and morphologies of the catalysts deposited on the Ni foam substrate were investigated via scanning electron microscopy (SEM) using a Tescan Lyra 3 high-resolution dual-beam focused ion beam scanning electron microscope. The elemental compositions of the samples were determined by energy-dispersive X-ray spectroscopy (EDS). The crystalline structures of the synthesized catalysts were analyzed by X-ray diffraction (XRD) using a Rigaku MiniFlex diffractometer (Japan) operated at 40 kV and 15 mA with Cu Kα radiation ($\lambda = 1.5406$Å).

2.7. Product Analysis. HMF conversion and FDCA yield were analyzed by HPLC (Shimadzu, Japan) using a C18 Shim Pack Velox column (2.7 μm, 50 ×2.1 mm) to determine the concentrations of HMF and its oxidation products, including FDCA, 5-hydroxymethyl-2-furancarboxylic acid (HMFCA), 2,5-diformylfuran (DFF), and 5-formyl-2-furancarboxylic acid (FFCA). The concentrations of HMF and the generated products were calculated from the HPLC calibration curves.

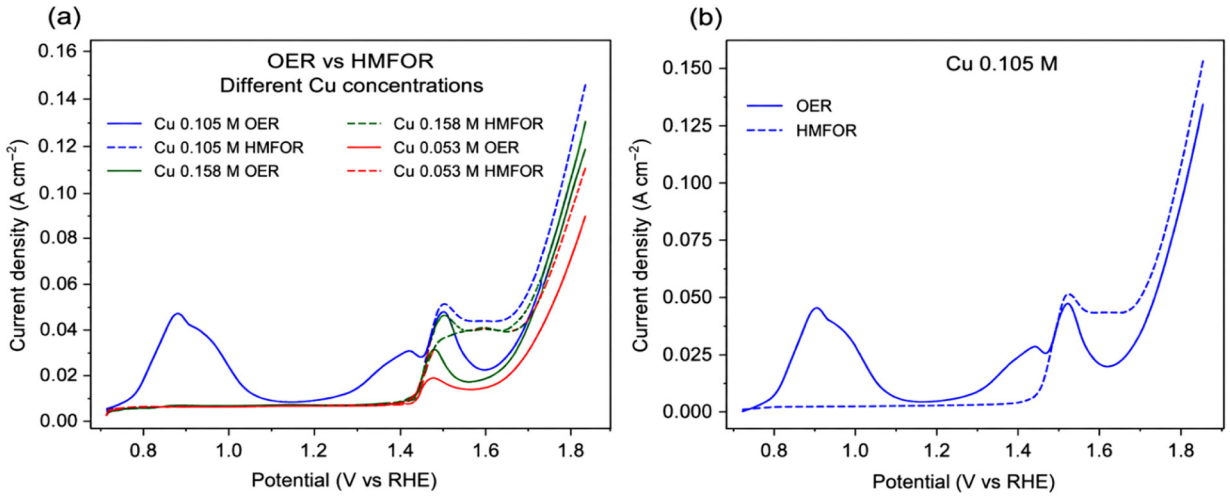


Figure 2. LSV curves comparing the OER and HMFOR performance of Cu-based electrodes prepared with (a) different Cu precursor concentrations and (b) 0.105 M Cu in 1 M KOH

HMF conversion and product yield were determined using Eqs. 1 and 2, respectively:

$$\text{HMF conversion}(\%) = \left(1 - \frac{\textit{Concentration of the remaining HMF}}{\textit{Concentration of the initial HMF}}\right) \times 100 \quad (1)$$

$$\textit{Product yield}\ (\%) = \frac{\textit{Concentration of product formed}}{\textit{Concentration of the initial HMF}} \times 100 \quad (2)$$

3. RESULTS AND DISCUSSION

3.1. Optimization of the Cu Concentration and Electrodeposition Potential. The effect of Cu concentration on the electrocatalytic performance of the resulting electrode was evaluated using LSV measurements, as shown in Figure 7 (a). Among the tested samples, those prepared with 0.105 M Cu exhibited the highest current density, indicating significantly enhanced catalytic activity compared with those obtained under other Cu concentrations. HMF introduction led to a noticeable increase in current density for all samples. This enhancement was most significant for the sample prepared with 0.105 M Cu, suggesting that this concentration was the most favorable for HMF oxidation.

As shown in Figure 2 (b), at a potential of ~1.6 V vs. RHE, the electrode prepared with 0.105 M Cu demonstrated a noticeable increase in current density. This increase became more pronounced with increasing potential, indicating the onset of oxidation. In the presence of HMF, the increase in current density for HMOR (dashed curve) was consistently higher than that for OER (solid curve) at the same applied potential.

Following optimization of the Cu concentration, the optimal applied potential was investigated (Figure 3 (a)). Different potentials (−0.5, −1.0, −1.5, and −2.0 V vs. RHE) were tested while the Cu concentration was fixed at 0.105 M. Compared with the catalysts prepared at other applied potentials, that prepared at −2.0 V vs. RHE exhibited the best performance, achieving a current density approaching ~0.23 A cm^{-2} at ~1.80 V vs. RHE during HMFOR.

This behavior is further confirmed in Figure 3 (b), which compares the performance of the sample prepared at the optimal potential (−2.0 V) for OER and HMFOR. A noticeable increase in current density was observed at potentials beyond ~1.41 V vs. RHE, indicating the onset of oxidation. In the presence of HMF, the current density at potentials beyond ~1.46 V vs. RHE was consistently higher for HMFOR than for OER; for instance, at ~1.6 V vs. RHE, the current density for HMFOR (~0.05 A cm^{-2}) was higher than that for OER. This result confirms that HMF addition enhances the electrochemical response by facilitating oxidation.

Although electrodeposition at −2.0 V produced electrodes with the best performance, electrodeposition at −1.5 V also resulted in electrodes with relatively good performance, rendering it a suitable alternative. This result can be attributed to the formation of a thinner deposition layer at a less negative potential, which may facilitate the exposure of active sites. A reduced layer thickness can improve accessibility and minimize the blockage of active sites, allowing for efficient interaction with the electrolyte[47,48].

3.1.1. Optimization of the Ni concentration. Further optimization was performed by investigating the optimal Ni precursor concentration. Three Ni concentrations of 0.053, 0.105, and 0.158 M were tested. As shown in Figure 4 (a), the electrode prepared with 0.158 M Ni exhibited the best electrochemical performance among the samples.

Unlike the behavior demonstrated by the Cu-based samples shown in Figures 2 and 3, no distinct peak was detected at the beginning of the OER after Ni deposition. This result suggests a distinct surface behavior in which the catalyst does not undergo a pronounced activation step. The onset potential for all samples was ~1.38 V vs. RHE. Upon HMF addition, a significant

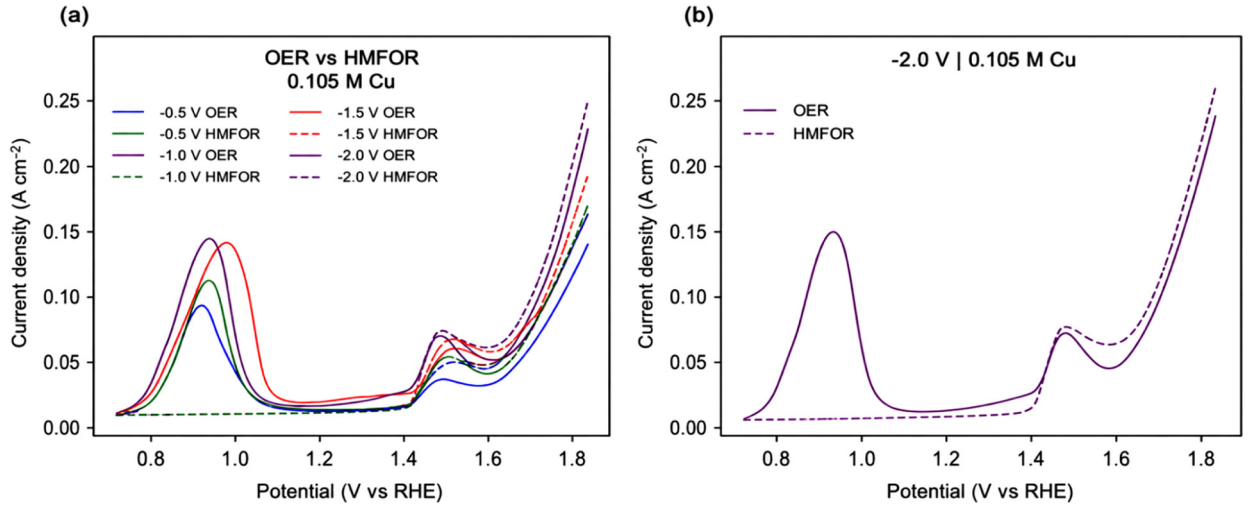


Figure 3. LSV curves showing the effect of the electrodeposition potential on the electrocatalytic performance of Cu-based electrodes (0.105 M Cu) in 1 M KOH during OER and HMFOR

increase in current density was observed for all electrodes prepared with all Ni concentrations, indicating enhanced catalytic activity toward HMFOR. The electrode prepared with the highest Ni concentration (0.158 M) showed the largest increase in current density.

Given these results, the highest Ni concentration was selected as the optimal condition for further experiments. 0.158 M Ni was mixed with 0.105 M Cu to evaluate the combined behavior of the metals, as shown in Figure 5. Interestingly, the results revealed the same pattern: increasing the Ni concentration led to higher current densities for both OER and HMFOR. Among the tested samples, the electrode prepared with 0.158 M Ni exhibited the best performance. These results confirm that the trend observed in the single-Ni system is preserved in the mixed Ni–Cu system, with higher Ni concentrations leading to improved catalytic performance.

3.2. Analysis of Catalyst Configurations. Different deposition strategies, including mixed-metal and LBL deposition (Ni followed by Cu and Cu followed by Ni), were compared to evaluate the effect of the catalyst configuration, as shown in Figure 6. Overall, all configurations exhibited comparable trends for both OER and HMFOR, particularly at higher potentials. However, noticeable differences in performance were observed when their current densities were compared for HMFOR.

Among the tested catalyst configurations, the Cu-followed-by-Ni LBL structure (Figure 7 (a)) demonstrated the highest current density, especially at higher potentials, indicating superior catalytic activity. The Ni-followed-by-Cu LBL configuration (Figure 7 (b)) showed slightly lower performance; the mixed-metal and pulse-assisted systems also exhibited comparatively lower current responses. These results suggest that the deposition sequence plays a significant role in determining catalytic behavior. Depositing Cu as the first layer, followed by Ni, may provide a more favorable surface structure or enhance the accessibility of active sites.

Compared with the single-metal systems, the Cu-only and Ni-only electrodes showed lower overall performance, confirming that the combination of these metals enhances catalytic activity owing to possible synergistic effects between Cu and Ni species. Although the differences between the electrode configurations were not extremely large, the Cu-followed-by-Ni LBL structure

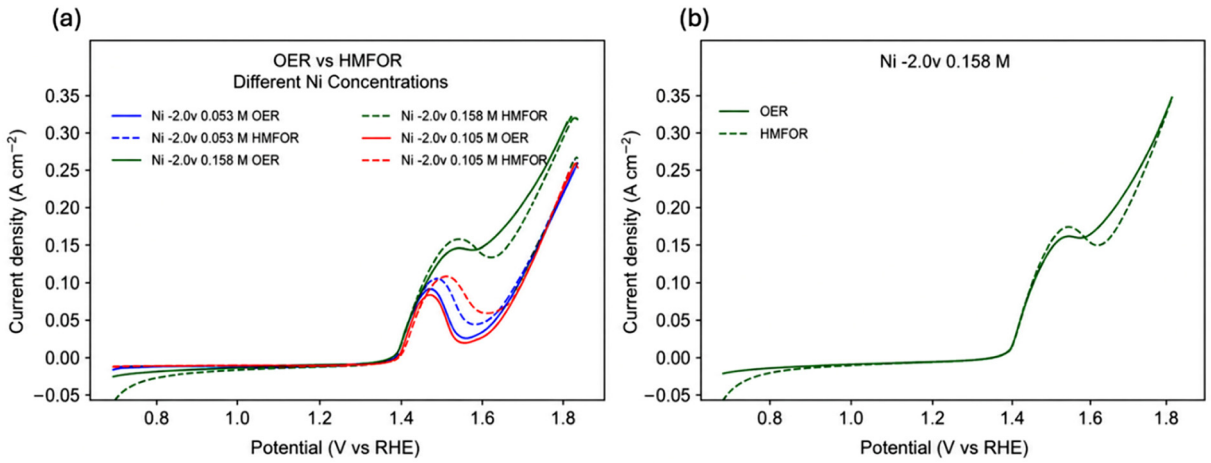


Figure 4. LSV curves comparing the OER and HMFOR performance of Ni-based electrodes prepared with (a) different Ni precursor concentrations and (b) 0.158 M Ni in 1 M KOH

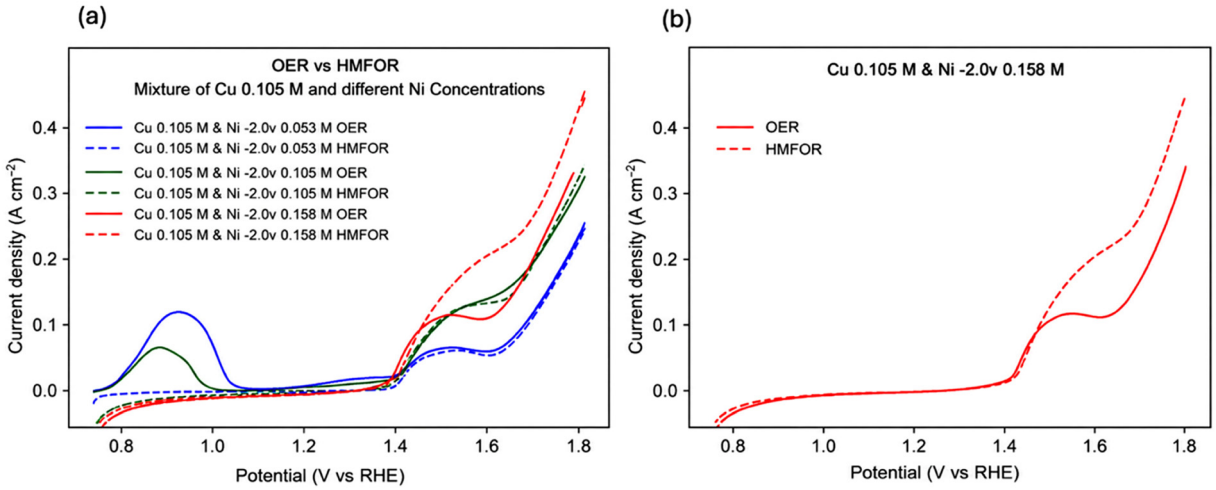


Figure 5. LSV curves comparing the OER and HMFOR performance of mixed Ni–Cu-based electrodes prepared with (a) different Ni precursor concentrations and (b) 0.158 M Ni in 1 M KOH

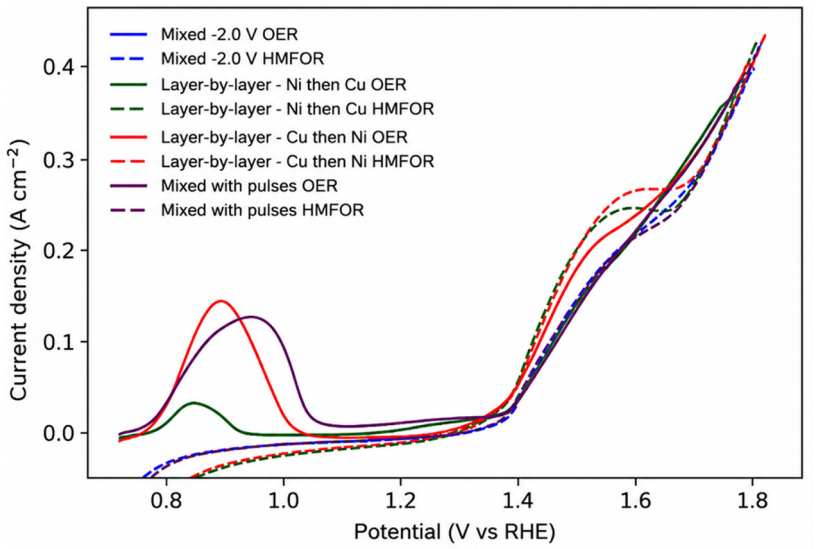


Figure 6. LSV curves comparing the OER and HMFOR performance of Ni- and Cu-based catalysts with different configurations in 1 M KOH

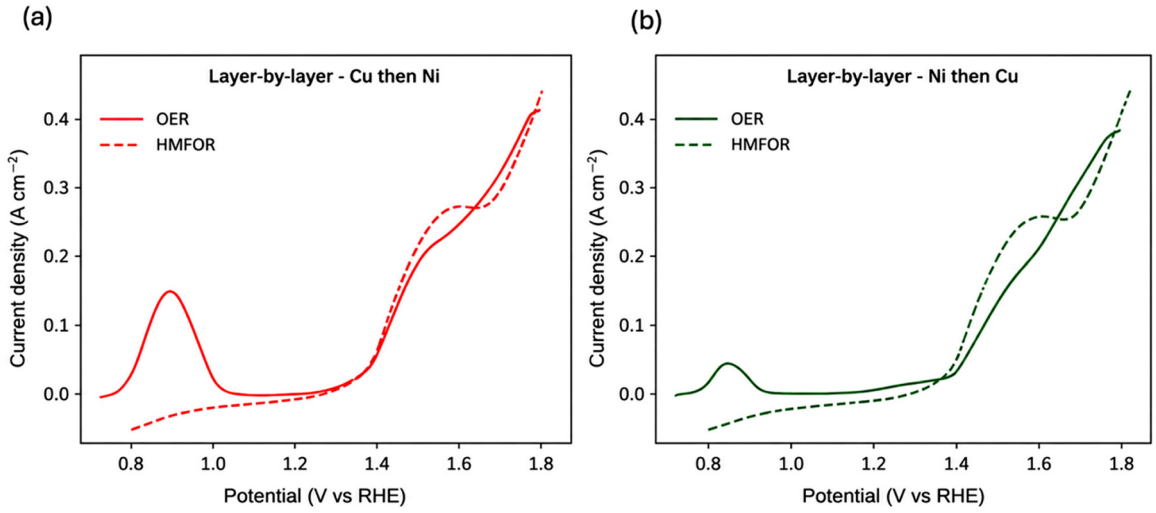


Figure 7. Comparison of the OER and HMFOR performance of LBL-deposited Ni–Cu-based catalysts in 1 M KOH: (a) Cu followed by Ni and (b) Ni followed by Cu

consistently showed the best performance across the tested conditions.

Based on the optimization results, further testing was carried out using electrodes prepared with a Cu-followed-by-Ni LBL configuration at the optimized metal concentrations (0.105 M Cu and 0.158 M Ni) and a constant potential of −2.0 V using a chronoamperometric method.

3.3. Long-term Electrochemical Performance and Stability. Electrodes with the Cu-followed-by-Ni LBL configuration were selected for further investigation based on the optimized parameters obtained from the initial screening. For the first electrode, a Cu layer was electrodeposited on the Ni foam substrate for 120 s at −1.5 V (vs. Ag/AgCl), followed by a Ni layer for 60 s under the same potential. A potential of −1.5 V was intentionally chosen to avoid excessive coverage, which could potentially block active sites and limit catalytic accessibility.

Considering the strong performance observed for the Cu-based electrodes during earlier optimization experiments, a second electrode was prepared with an extended Cu deposition time. For this electrode, the Cu layer was deposited for 400 s, followed by the Ni layer for 60 s. This modification was introduced to enhance the contribution of Cu to the catalytic system, while maintaining the role of Ni as a secondary active phase.

Ultimately, this configuration (400 s for Cu deposition/60 s for Ni deposition) was selected as a representative sample for further analysis, and its electrochemical performance was investigated.

The experimental procedure began with CV. This step is essential for activating and conditioning the catalyst surface prior to further measurements. During CV, surface transformations occur, promoting the formation of active catalytic species such as NiOOH, while simultaneously removing impurities and improving the surface organization. Hence, the number of active sites increases and the electrode becomes more stable and electrochemically ready. Initially, 50 CV cycles were conducted to ensure sufficient surface activation. Thereafter, the electrode exhibited stable behavior, indicating that the activation process was complete. As illustrated in Figure 8, 10 additional cycles were performed to further confirm the stability of the electrode. The consistency observed in these cycles confirmed that the electrode surface reached a stable state suitable for subsequent electrochemical measurements.

OCP measurements were performed to evaluate the intrinsic behavior of the electrochemical system without an external potential or current. In this test, the electrode was allowed to reach its natural equilibrium state to provide insights into its stability and surface conditions. As shown in Figure 9, the system exhibited a gradual decrease in potential during the first 300 s, reflecting the behavior of the electrode before HMF addition. After HMF introduction, the potential demonstrated a clear and sudden negative shift, followed by a gradual decrease until a nearly stable value was reached. The difference in potentials before and after HMF addition indicates that HMF directly affects the interfacial electrochemical behavior of the electrode. Therefore, the addition of HMF changes the surface environment of the electrode, leading to the establishment of a new electrochemical equilibrium. These findings support the enhanced oxidation behavior observed in the electrochemical measurements.

Figure 10 illustrates the LSV curves of the Ni–Cu electrode. After HMF addition, the current density increased and the onset potential noticeably shifted toward lower values. Specifically, the onset potential decreased from ~1.39 V vs. RHE for OER to ~1.36 V vs. RHE for HMFOR, indicating enhanced catalytic activity in the presence of HMF. This behavior suggests that HMFOR is kinetically more favorable than OER, as reflected by both the lower onset potential and higher current density. Moreover, the increased current response at higher potentials supports improvements in electrocatalytic performance and may indicate more efficient HMF conversion.

Tafel plots are commonly used to evaluate the kinetics of electrochemical reactions by analyzing the relationship between the overpotential (η) and the logarithm of the current density ($\log(j)$). This relationship is derived from the Butler–Volmer equation and, in the kinetically controlled region, can be simplified to the Tafel equation (Eq. 3):

$$\eta = a + b\log(j) \tag{3}$$

The Tafel equation provides a simple means to describe how the reaction rate responds to an increase in applied potential. In particular, the Tafel slope (b) reflects the additional potential required to increase the current density by one order of magnitude; thus, it indicates the ease of electron transfer during the reaction. Lower slopes generally correspond to faster kinetics, whereas higher slopes suggest more complex or slower reaction pathways. In practice, Tafel analysis is applied only within the linear region of the η vs. $\log(j)$ curve, where the reaction is controlled by charge transfer.

As the current increased, the overpotential gradually increased, reflecting a transition toward the kinetically controlled region. A nearly linear segment can be observed before the curves begin to deviate at higher current densities, where mass-transport effects and possible surface changes may influence the response. The linear region used for Tafel analysis is shown in the Figure 11.

As shown in Figure 11, the Tafel slopes were determined to be 57.4 mV dec^{-1} for OER and 62.9 mV dec^{-1} for HMFOR. The slightly higher slope for HMFOR suggests marginally slower apparent charge-transfer kinetics compared with OER. However, the difference is small, indicating that the catalyst is able to drive HMFOR with comparable kinetic behavior despite the involvement of a more complex reaction pathway.

EIS was used to understand the interfacial charge-transfer behavior and reaction kinetics of the Ni–Cu electrode. In a typical Nyquist plot, a well-defined semicircle in the high-frequency region is associated with the charge-transfer resistance (R_{ct}), and a smaller semicircle indicates faster electron transfer. However, deviations from the ideal semicircle are commonly observed in complex electrocatalytic systems owing to the contribution of additional processes such as adsorption and diffusion. As shown in Figure 12, EIS measurements were conducted with and without HMF at different applied potentials (0.55, 0.60, and 0.65 V) to evaluate the influence of the reaction conditions on the electrochemical behavior of the electrode.

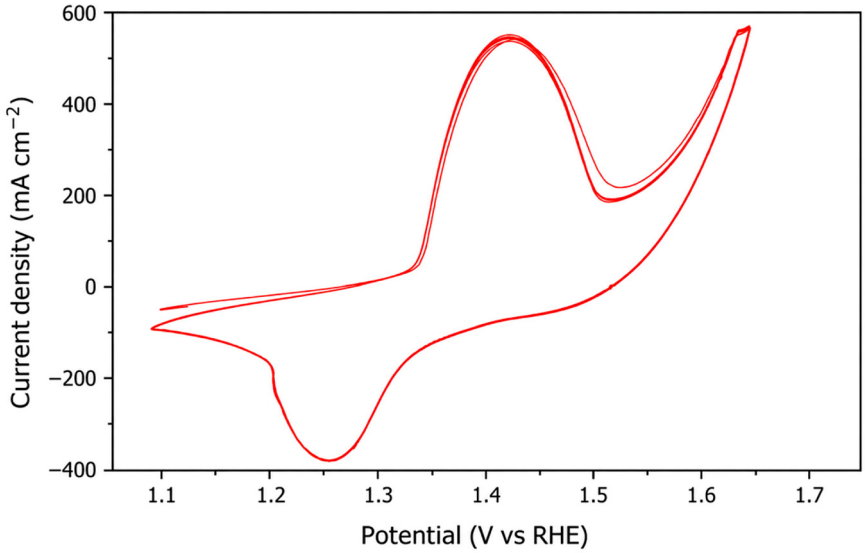


Figure 8. Curves of the last 10 CV cycles of the Ni–Cu electrode

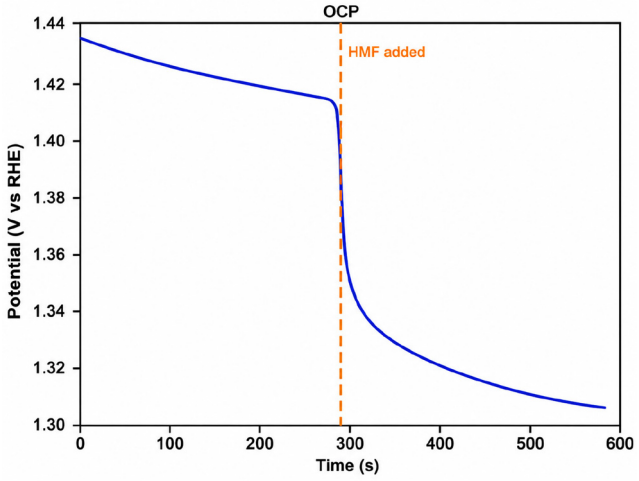


Figure 9. OCP measurements of the Ni–Cu electrode

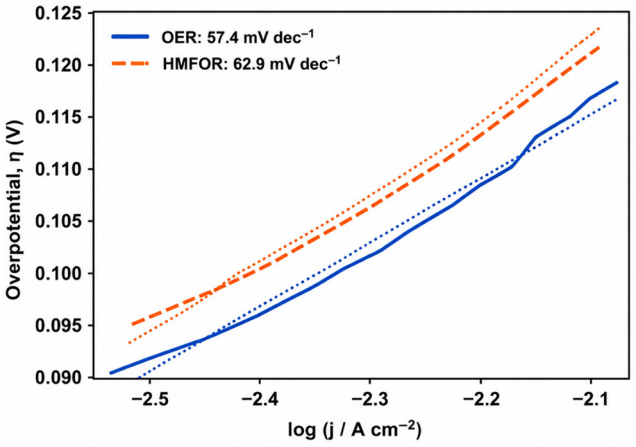


Figure 11. Enlarged view of the linear region used for Tafel-slope determination

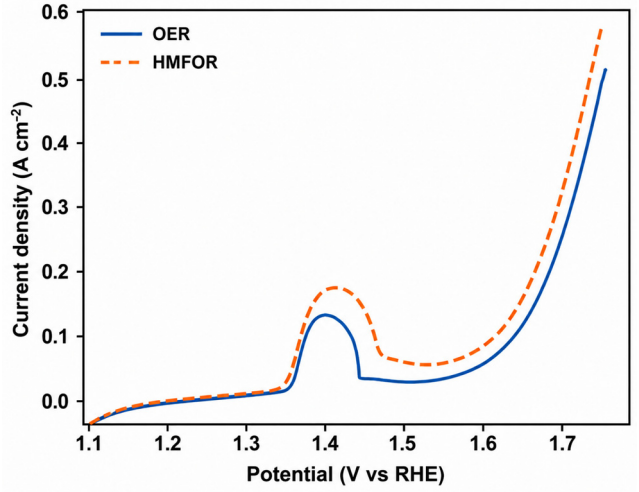


Figure 10. LSV curves comparing the OER and HMFOR performance of the Ni–Cu electrode in 1 M KOH

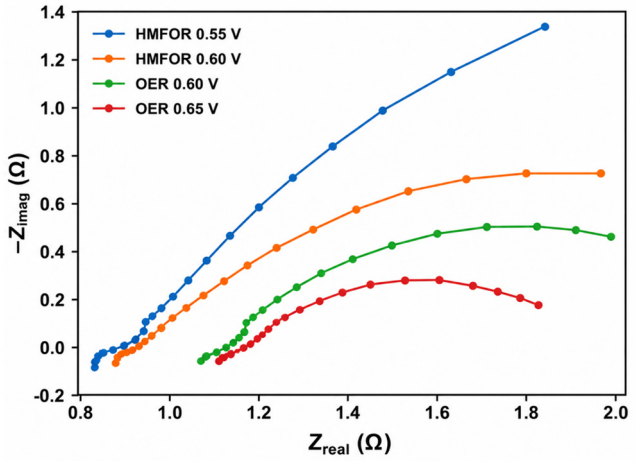


Figure 12. Nyquist plots obtained with and without HMF at different applied potentials

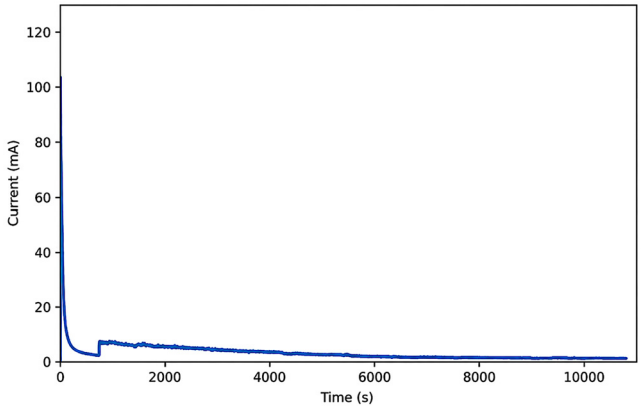


Figure 13. Evaluation of the stability of the LBL-deposited Ni–Cu catalyst by CA at a constant potential of 1.43 V vs. RHE over a 3 h period

A comparison of the high-frequency region revealed differences in the impedance response between the samples. Specifically, the curves recorded with HMF shifted toward lower Z_{real} values compared with those recorded without HMF, indicating reduced interfacial resistance and enhanced charge-transfer kinetics in the presence of HMF.

For HMFOR, the impedance response decreased with increasing potential, with the curve recorded at 0.60 V showing the lowest impedance, suggesting improved charge-transfer behavior and faster reaction kinetics. Without HMF, a similar trend was observed, with the impedance decreasing at a higher potential and 0.65 V exhibiting the lowest response. However, the impedance values remained higher than those obtained in the presence of HMF, indicating slower kinetics in the absence of HMF.

Chronoamperometry (CA) was performed at a fixed potential of 1.43 V vs. RHE in 1.0 M KOH for 3 h to assess the long-term behavior of the electrode during HMFOR. As shown in Figure 13, the current sharply dropped within the first few seconds of the reaction; this phenomenon is commonly associated with non-Faradaic double-layer charging at the electrode surface. Subsequently, a slight increase in current density was observed. This behavior may be attributed to the gradual activation of the catalyst surface and the formation of active species during the reaction. Thereafter, the current stabilized and remained relatively constant over the rest of the measurement period, indicating that the system reached a steady state dominated by the electrochemical reaction. The stable current over time suggests that the catalyst maintains its activity during continuous operation. The minor variations in current may be associated with changes in mass transport or the gradual formation of surface intermediates.

3.4. Structural and Morphological Characterization.

A series of Ni–Cu-based electrodes was synthesized using different deposition strategies, including single-metal, mixed-metal, and LBL deposition, and the effects of the precursor concentration, deposition potential, and deposition mode (continuous vs. pulsed) were systematically investigated to identify the optimal electrodeposition conditions.

The surface morphologies of the prepared Ni–Cu electrodes are shown in Figure 14. The optimized mixed-metal sample (Figure 14 (a)) shows a flake- or sheet-like structure with a surface consisting of relatively flat and irregular features. By contrast, the optimized LBL sample (Figure 14 (b)) exhibits a more clustered morphology, with the particles forming flower- or cauliflower-like aggregates distributed over the electrode surface. The Ni foam structure is partially visible in both samples, indicating that the deposited metal layer does not form a completely smooth film. This difference in morphology suggests that the deposition method affects how the catalyst is distributed on the substrate surface.

EDS was used to examine the elemental compositions of the optimized mixed-metal- and LBL-deposited catalysts. The dominant element detected in the mixed-metal-deposited sample was Cu (75.23 at.%), followed by O (16.82 at.%) and Ni (7.95 at.%). The higher O content compared with Ni suggests the formation of oxidized surface species, which is consistent with the oxidized nature of the sample. The LBL-deposited sample also showed a Cu-rich (83.76 at.%) outer surface owing to the deposited Cu layer, along with small amounts of Ni (3.87 at.%) and O (12.37 at.%).

Considering that LBL deposition began with Cu followed by Ni, Cu surprisingly emerged as the dominant element in the EDS analysis. This unexpected result can be attributed to several factors, including the surface-sensitive nature of EDS with a limited penetration depth. If the Ni layer is relatively thin, nonuniform, or partially porous, the underlying Cu layer may still contribute to the detected signals. The dominance of Cu suggests that the Cu layer is either more continuous, thicker, or more exposed than the overlying Ni layer. Thus, the measured composition reflects the level of surface exposure rather than the designed layer sequence. The results indicate that the substrate surface was mainly covered by the Cu layer, limiting the exposure of the Ni foam underneath.

An LBL-deposited electrode was prepared using modified electrodeposition parameters to further investigate the influence of the deposition conditions on the LBL structure. For this electrode, a potential of −1.5 V was applied, the Cu deposition time was extended to 400 s, and the Ni deposition time was reduced to 60 s. The surface morphology of the resulting electrode was then characterized using SEM, as shown in Figure 15. The electrode revealed a relatively rough and nonuniform surface with clustered features, suggesting that the deposited layers formed agglomerated or partially porous structures rather than a continuous film.

The EDS spectrum in Figure 16 reveals the presence of O, Ni, and Cu on the electrode surface. Cu emerged as the dominant element, with an atomic percentage of 83.76 at.%. Oxygen was detected at an atomic percentage of 12.37 at.%, suggesting the presence of O-containing surface species, likely because of the partial surface oxidation of the deposited layer. Signals indicative of Ni, which was detected with an atomic percentage of 3.87 at.%, were also observed, indicating that Ni remains present but is less exposed compared with Cu on the electrode surface. The high Cu content suggests that the outer deposited layer is mainly Cu-rich, whereas the low Ni content may be due to surface coverage by Cu species and the low Ni deposition time, resulting in a thin Ni layer.

Figure 17 shows the X-ray diffraction pattern of the electrode prepared under modified LBL conditions. The prominent peaks

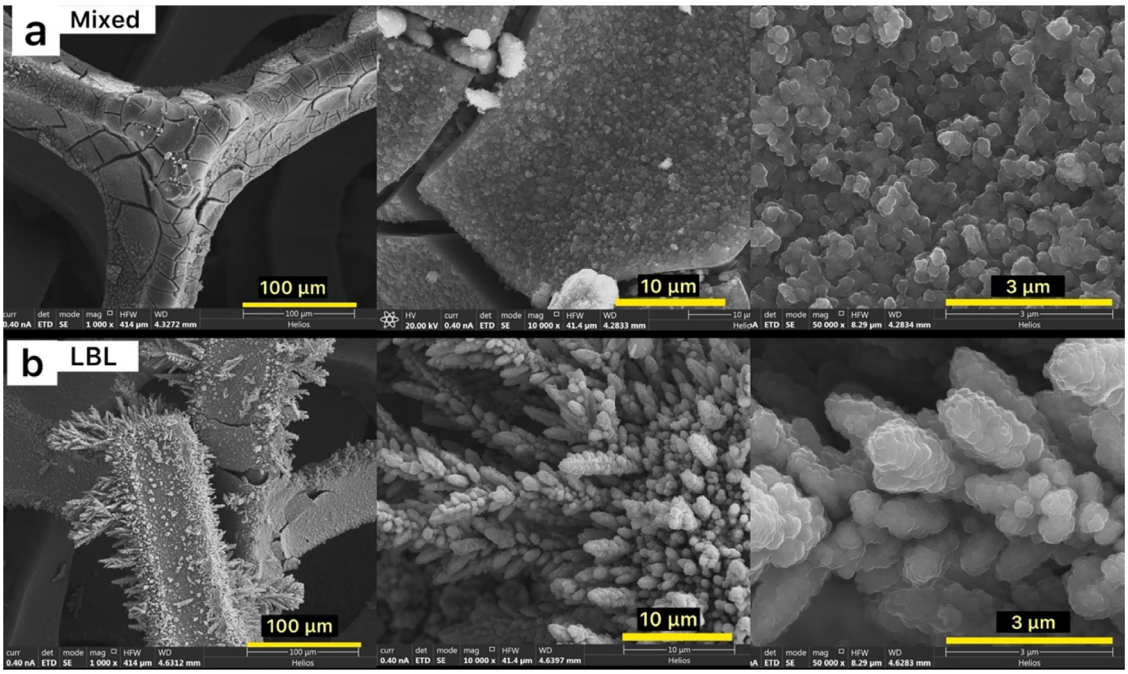


Figure 14. SEM images of the surface of Ni–Cu electrodes prepared using (a) mixed-metal and (b) LBL deposition

observed at approximately 44.5°, 51.8°, and 76.4°can be indexed to the (111), (200), and (220) crystallographic planes of metallic Ni, respectively, and originate from the Ni foam substrate, indicating its highly crystalline nature. No additional peaks corresponding to the deposited Ni–Cu layer are observed, suggesting that the deposited layer is either amorphous, present with low crystallinity, or deposited with a relatively low loading and thin surface coverage. Some Cu/Ni systems reported in the literature show weak or unresolved deposited-layer peaks owing to overlap with the substrate signal and limited diffraction intensity. The minor broad features with low intensities may be attributed to surface species or poorly crystalline phases formed during electrodeposition. Therefore, the XRD pattern confirms the crystalline Ni foam background but does not clearly resolve the deposited Ni layer.

3.5. Mechanism and Product Analysis. Based on previously reported HMF oxidation pathways[30,48], as shown in

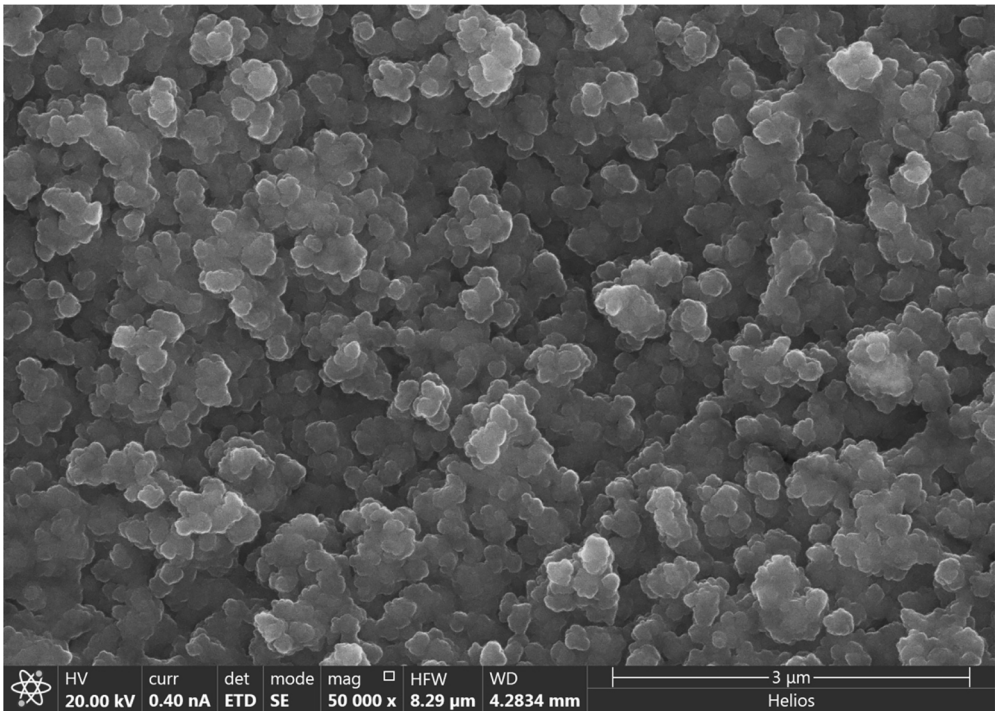


Figure 15. SEM image of the surface of the LBL-deposited Ni–Cu electrode prepared under modified deposition conditions

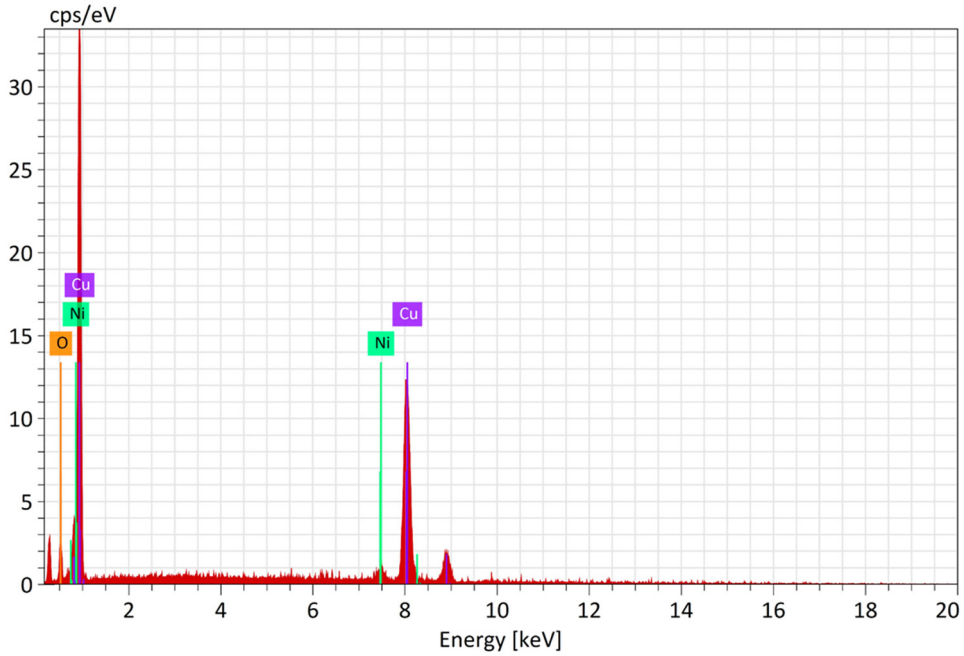


Figure 16. EDS spectrum of the LBL-deposited Ni–Cu electrode prepared under modified deposition conditions

Figure 18, HMF oxidation proceeds via two routes, depending on whether the hydroxymethyl or aldehyde group is oxidized first. Both pathways converge during the formation of FFCA, which is subsequently oxidized to FDCA. In Route 1, the aldehyde group (–CHO) of HMF is first oxidized to form DFF, followed by further oxidation to FFCA and, finally, FDCA. This pathway is commonly associated with an indirect mechanism in which NiOOH facilitates the oxidation of aldehyde groups, which is often considered the rate-determining step. In Route 2, the hydroxymethyl group ($–CH_2OH$) is first oxidized, forming HMFCA. The HMFCA intermediate is then further oxidized to FFCA and, finally, FDCA. This pathway typically involves potential-dependent oxidation and proceeds via similar proton-coupled electron transfer steps.

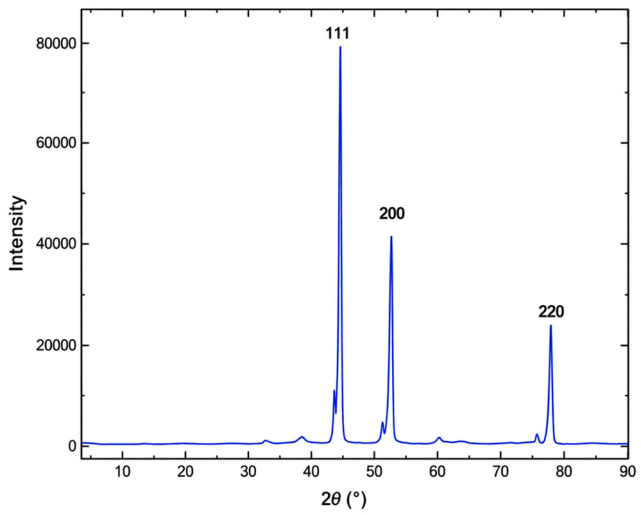


Figure 17. XRD pattern of the LBL-deposited Ni–Cu electrode prepared under modified conditions

Overall, both oxidation pathways may occur depending on the catalyst surface and reaction conditions. Further insights into the dominant pathway can be obtained through HPLC analysis by identifying the key intermediate products (DFF, HMFCA, and FFCA), as their presence reflects the sequence of oxidation steps during HMF conversion[49].

3.6. HMF Conversion and FDCA Yield. HPLC was used to monitor the reaction progress via measurements of the remaining HMF and the amount of FDCA formed. Calibration curves for HMF and FDCA were prepared using standard solutions of known concentrations. The good linearity of the calibration curves, with R^2 values of 0.994 for HMF and 0.9948 for FDCA, confirmed their validity for estimating concentrations from the HPLC peak areas.

The HPLC results showed that HMF conversion increased with the reaction time and reached approximately 95% after 120 min, indicating that most of the HMF was consumed during the reaction. However, the FDCA yield was only ~50%, suggesting that not all of the consumed HMF was directly converted to FDCA. This finding is consistent with the second proposed reaction pathway discussed in Section 3.5, where part of the HMF is converted to intermediate products, such as HMFCA and FFCA, before becoming completely oxidized to FDCA. Thus, although the catalyst shows good HMF conversion efficiency, further optimization is required to improve the selectivity of the electrode toward FDCA. Future studies should explore a wider range of operating conditions, conduct extended stability tests, and employ advanced characterization methods to gain a deeper understanding of the HMF oxidation mechanism.

4. CONCLUSION

In this study, the effects of various electrodeposition parameters on the performance of Cu-, Ni-, and Cu-Ni-based catalysts for

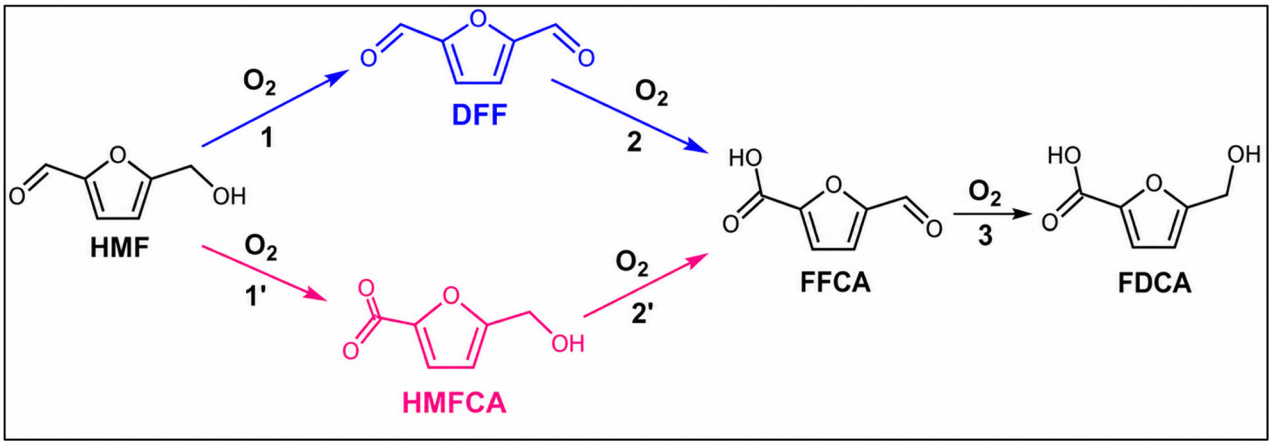


Figure 18. Proposed reaction pathways for the electrochemical oxidation of HMF to FDCA (Reproduced with permission from Barnwal et al.[50])

HMF electrooxidation were investigated to understand how the metal concentration, deposition conditions, and catalyst configuration influence the catalytic behavior for OER and HMFOR.

Although both Cu and Ni showed reasonable activity individually, the combination of the two metals resulted in noticeably better performance, suggesting a synergistic interaction between them. Among the catalyst configurations investigated, the LBL structure consistently showed the best overall behavior, particularly when Cu was deposited as the first layer, followed by Ni. The LSV results showed a clear increase in current upon HMF addition, indicating that the catalyst favors HMFOR over OER. Tafel analysis suggested moderate reaction kinetics, while the EIS results indicated improved charge-transfer behavior in the presence of HMF, aligning with the observed enhancement in catalytic performance. Overall, the results highlight that combining Cu with Ni, particularly in a LBL configuration, provides better performance than using either metal alone. This finding suggests that further optimization should focus on this combination and configuration.

Future work can focus on the conversion of HMF to FDCA at different potentials to determine the optimal potential, as well as the detailed identification of HMF oxidation intermediates and final products. Optimization of the LBL structure and improvement of the interaction between Cu and Ni may also be attempted to enhance the overall performance and stability of the resulting catalysts.

AFFILIATIONS AND AUTHOR DETAILS

Undergraduate Author

Hussa Naji Alwohaibi – *Department of Chemical Engineering, King Fahd University of Petroleum & Minerals, Dhahran 31261, Saudi Arabia;* 0009-0008-7346-6887
Email: S202279600@kfupm.edu.sa

Corresponding Author

Wasif Farooq – *Research Mentor, Associate Professor, Department of Chemical Engineering, King Fahd University of Petroleum & Minerals, Dhahran 31261, Saudi Arabia;* 0000-0002-4882-0097
Email: wasif@kfupm.edu.sa

ACKNOWLEDGEMENTS

The authors acknowledge the support provided by the Chemical Engineering and Chemistry Departments at the King Fahd University of Petroleum and Minerals. The authors also extend their appreciation to the technical staff and laboratory team for their assistance with sample preparation and testing. Special thanks are extended to Dr. Akilarasan Muthumariappan, a postdoctoral researcher, for his valuable training, continuous guidance, and support throughout this project, which greatly contributed to the completion of this study.

REFERENCES

(1) Lopez, G., Keiner, D., Fasihi, M., Koiranen, T. & Breyer, C. [1] From fossil to green chemicals: sustainable pathways and new carbon feedstocks for the global chemical industry. *Energy Environ. Sci.* **16**, 2879–2909 (2023).

(2) Abas, N., Kalair, A. & Khan, N. [2] Review of fossil fuels and future energy technologies. *Futures* **69**, 31–49 (2015).

(3) Roy, D., Dey, A. K., Mandal, A. & Kamila, B. [3] A comprehensive review on the sustainable approach of fossil-based polymers toward bio-based polymers. *Polym. Bull.* **82**, 11625–11696 (2025).

(4) Belboom, S. & Léonard, A. [4] Does biobased polymer achieve better environmental impacts than fossil polymer? Comparison of fossil HDPE and biobased HDPE produced from sugar beet and wheat. *Biomass Bioenergy* **85**, 159–167 (2016).

(5) OECD. [5] Global Plastics Outlook: Policy Scenarios to 2060 *OECD* https://www.oecd.org/en/publications/global-plastics-outlook_aa1edf33-en.html (2022) doi:10.1787/aa1edf33-en.

(6) Tilsted, J. P. & Newell, P. [6] Synthetic transitions: the political economy of fossil fuel as feedstock. *Rev. Int. Polit. Econ.* **32**, 1214–1238 (2025).

(7) Ioelovich, M. [7] Recent findings and the energetic potential of plant biomass as a renewable source of biofuels - A review. *BioResources* **10**, 1879–1914 (2015).

(8) THE CHEMISTRY OF PETROLEUM.

(9) A-Review-on-Petroleum-Source-Uses-Processing-Products-and-the-Environment.pdf.

(10) Morenov, V., Leusheva, E., Buslaev, G. & Gudmestad, O. T. [12] System of Comprehensive Energy-Efficient Utilization of Associated Petroleum Gas with Reduced Carbon Footprint in the Field Conditions. *Energies* **13**, (2020).

(11) Venkatesh, A., Jaramillo, P., Griffin, W. M. & Matthews, H. S. [13] Uncertainty Analysis of Life Cycle Greenhouse Gas Emissions from Petroleum-Based Fuels and Impacts on Low Carbon Fuel Policies. *Environ. Sci. Technol.* **45**, 125–131 (2011).

(12) [14] CO2 emission and air pollution (volatile organic compounds, etc.)–related problems causing climate change. in *Current Trends and Future Developments on (Bio-) Membranes* 1–30 (Elsevier, 2020). doi:10.1016/B978-0-12-816778-6.00001-1.

(13) Hao, Y., Chen, H., Wei, Y.-M. & Li, Y.-M. [15] The influence of climate change on CO2 (carbon dioxide) emissions: an empirical estimation based on Chinese provincial panel data. *J. Clean. Prod.* **131**, 667–677 (2016).

(14) Zhang, Z., Zhang, J. & Feng, Y. [16] Assessment of the Carbon Emission Reduction Effect of the Air Pollution Prevention and Control Action Plan in China. *Int. J. Environ. Res. Public. Health* **18**, (2021).

(15) Mori, R. [17] Replacing all petroleum-based chemical products with natural biomass-based chemical products: a tutorial review. *RSC Sustain.* **1**, 179–212 (2023).

(16) Belaïd, F., Boubaker, S. & Kafrouni, R. [18] Carbon emissions, income inequality and environmental degradation: The case of Mediterranean countries. *Eur. J. Comp. Econ. EJCE* **17**, 73–102 (2020).

(17) Ajeigbe, K. B. & Ganda, F. [19] The Impact of Pollution and Carbon Emission Control on Financial Development, Environmental Quality, and Economic Growth: A Global Analysis. *Sustainability* **16**, (2024).

(18) Unegg, M. C., Steininger, K. W., Ramsauer, C. & Rivera-Aguilar, M. [20] Assessing the environmental impact of waste management: A comparative study of CO2 emissions with a focus on recycling and incineration. *J. Clean. Prod.* **415**, 137745 (2023).

(19) Keim, W. Petrochemicals: Raw material change from fossil to biomass? *Pet. Chem.* **50**, 298–304 (2010).

(20) Schilling, M. & Chiang, L. [8] The effect of natural resources on a sustainable development policy: The approach of non-sustainable externalities. *Energy Policy* **39**, 990–998 (2011).

(21) Mufutau Opeyemi, B. [11] Path to sustainable energy consumption: The possibility of substituting renewable energy for non-renewable energy. *Energy* **228**, 120519 (2021).

(22) He, H. *et al.* Functional Carbon from Nature: Biomass-Derived Carbon Materials and the Recent Progress of Their Applications. *Adv. Sci.* **10**, 2205557 (2023).

(23) Khandaker, T. *et al.* Biomass-derived carbon materials for sustainable energy applications: a comprehensive review. *Sustain. Energy Fuels* **9**, 693–723 (2025).

(24) Kohli, K., Prajapati, R. & Sharma, B. K. Bio-Based Chemicals from Renewable Biomass for Integrated Biorefineries. *Energies* **12**, (2019).

(25) Anastassiadis, S. G. CARBON SOURCES FOR BIOMASS, FOOD, FOSSILS, BIOFUELS AND BIOTECHNOLOGY - REVIEW ARTICLE. *World J. Biol. Biotechnol.* **1**, 1–32 (2016).

(26) Olah, G. A., Prakash, G. K. S. & Goeppert, A. Anthropogenic Chemical Carbon Cycle for a Sustainable Future. *J. Am. Chem. Soc.* **133**, 12881–12898 (2011).

(27) Menegazzo, F., Ghedini, E. & Signoretto, M. 5-Hydroxymethylfurfural (HMF) Production from Real Biomasses. *Molecules* **23**, (2018).

(28) Zhao, H., Holladay, J. E., Brown, H. & Zhang, Z. C. Metal Chlorides in Ionic Liquid Solvents Convert Sugars to 5-Hydroxymethylfurfural. *Science* **316**, 1597–1600 (2007).

(29) Bozell, J. J. & Petersen, G. R. Technology development for the production of biobased products from biorefinery carbohydrates—the US Department of Energy's "Top 10" revisited. *Green Chem.* **12**, 539–554 (2010).

(30) Aranha, D. J. & Gogate, P. R. A Review on Green and Efficient Synthesis of 5-Hydroxymethylfurfural (HMF) and 2,5-Furandicarboxylic Acid (FDCA) from Sustainable Biomass. *Ind. Eng. Chem. Res.* **62**, 3053–3078 (2023).

(31) He, O., A. Smith, B., Champange, P., G. Jessop, P. & Yu, H. How to make furfural and HMF production greener? Lessons from life cycle assessments. *Green Chem.* **27**, 14436–14477 (2025).

(32) F. Sousa, A. *et al.* Recommendations for replacing PET on packaging, fiber, and film materials with biobased counterparts. *Green Chem.* **23**, 8795–8820 (2021).

(33) Mulder, K. F. Sustainable Consumption and Production of Plastics? *Technol. Forecast. Soc. Change* **58**, 105–124 (1998).

(34) Bio-Plastics - An Alternative to Petroleum Based Plastics. *Int. J. Res. Stud. Agric. Sci.* **4**, (2018).

(35) (PDF) Nano-Cellulose Derived Bioplastic Biomaterial Data for Vehicle Bio-Bumper from Banana Peel Waste Biomass. *ResearchGate* https://doi.org/10.1016/j.dib.2016.05.029 (2025) doi:10.1016/j.dib.2016.05.029.

(36) Wei, Z., Li, W., Yuan, F., Sun, W. & Zhao, L. Kinetic Modeling of Homogenous Catalytic Oxidation of 5-Hydroxymethylfurfural to 2,5-Furandicarboxylic Acid. *Ind. Eng. Chem. Res.* **61**, 18352–18361 (2022).

(37) Meng, Z.-Z., Chen, S.-S., Li, H.-R. & He, L.-N. Heterogeneous Catalysis for Aerobic Oxidation of 5-Hydroxymethylfurfural to 2,5-Furandicarboxylic Acid under Base-Free Conditions. *ChemCatChem* **17**, e202401658 (2025).

(38) Xing, L., Jin, J., Xu, M., Bai, H. & Li, Z. Substrate Adsorption and Oxidation Synergistic Effect in Cu-Ni Bimetallic Catalyst for 5-Hydroxymethylfurfural Oxidation. *Catal. Lett.* **155**, 380 (2025).

(39) Zhang, J. *et al.* Boosting HMF oxidation performance via decorating ultrathin nickel hydroxide nanosheets with amorphous copper hydroxide islands. *J. Mater. Chem. A* **9**, 9685–9691 (2021).

(40) Li, Y. *et al.* Construction of hierarchical NiCu-based bimetallic electrocatalysts for promoting the electrooxidation of biomass derivatives. *Sustain. Energy Fuels* **7**, 4505–4513 (2023).

(41) Yang, G. *et al.* In-situ chemical corrosive nickel foam as high-efficient electrocatalyst for 5-hydroxymethylfurfural oxidation. *Appl. Surf. Sci.* **594**, 153432 (2022).

(42) Hou, Z., Wu, Y., Cao, W. & Wang, C. Construction of NiCu heterojunctions for highly efficient and profitable electrooxidation of HMF to FDCA: The indications from techno-economic analysis. *Appl. Catal. B Environ. Energy* **382**, 125938 (2026).

(43) Liu, J. *et al.* Synergistically enhanced co-adsorption of OH- and HMF on Cu-modified Ni aerogel for biomass upgrading coupled with hydrogen production. *Chem. Eng. J.* **525**, 169807 (2025).

(44) Woo, J. *et al.* Collaborative Electrochemical Oxidation of the Alcohol and Aldehyde Groups of 5-Hydroxymethylfurfural by NiOOH and Cu(OH)2 for Superior 2,5-Furandicarboxylic Acid Production. *ACS Catal.* **12**, 4078–4091 (2022).

(45) Nam, D.-H., Taitt, B. J. & Choi, K.-S. Copper-Based Catalytic Anodes To Produce 2,5-Furandicarboxylic Acid, a Biomass-Derived Alternative to Terephthalic Acid. *ACS Catal.* **8**, 1197–1206 (2018).

(46) Sajid, M., Zhao, X. & Liu, D. Production of 2,5-furandicarboxylic acid (FDCA) from 5-hydroxymethylfurfural (HMF): recent progress focusing on the chemical-catalytic routes. *Green Chem.* **20**, 5427–5453 (2018).

(47) Trotochaud, L., Young, S. L., Ranney, J. K. & Boettcher, S. W. Nickel–Iron Oxyhydroxide Oxygen-Evolution Electrocatalysts: The Role of Intentional and Incidental Iron Incorporation. *J. Am. Chem. Soc.* **136**, 6744–6753 (2014).

(48) Chen, S. *et al.* Reaction Mechanism and Kinetics of the Liquid-Phase Oxidation of 5-Hydroxymethylfurfural to 2,5-

Furandicarboxylic Acid. *Ind. Eng. Chem. Res.* **60**, 16887–16898 (2021).

(49) Aranha, D. J. & Gogate, P. R. A Review on Green and Efficient Synthesis of 5-Hydroxymethylfurfural (HMF) and 2,5-Furandicarboxylic Acid (FDCA) from Sustainable Biomass. *Ind. Eng. Chem. Res.* **62**, 3053–3078 (2023).

(50) Barnwal, P. K., Gurrala, R. C. & Peela, N. R. Tailored Octahedral Site Engineering in Spinel NiMnxCo2–xO4 Oxides for Base-Free Aerobic Oxidation of 5-Hydroxymethylfurfural to 2,5-Furandicarboxylic Acid in an Aqueous Medium. *ACS Sustain. Chem. Eng.* https://doi.org/10.1021/acssuschemeng.6c00980 (2026) doi:10.1021/acssuschemeng.6c00980.